Materials Horizons

ROYAL SOCIETY OF CHEMISTRY

COMMUNICATION

View Article Online
View Journal | View Issue

Cite this: *Mater. Horiz.*, 2026, **13**, 3868

Received 12th July 2025,
Accepted 21st January 2026

DOI: 10.1039/d5mh01319d

rsc.li/materials-horizons

Physically reconfigurable synaptic plasticity and learning in stretchable neuromorphic systems

Seung-Woo Lee, †[a] Kwan-Nyeong Kim,†[a] Sangjun Ma,†[a] Solji Ahn,[a] Dongsu Choi,[a] Min-Jun Sung,[a] Chae-Yun Song,[a] Jeong-Yun Sun *[ab] and Tae-Woo Lee *[abcd]

Wearable electronics that use intrinsically stretchable organic neuromorphic devices offer a promising approach to achieve human-like on-device processing with a seamless human body interface. A central challenge, however, lies in achieving tunable synaptic plasticity within the neuromorphic systems for endowing task-adaptable functions for broad and versatile applications, because synaptic plasticity is typically hardwired by the structural configuration of conventional devices. Here, we present a physically reconfigurable neuromorphic transistor platform enabled by an ion-conductive adhesive elastomer (IAE) that ensures robust mechanical integration and electrolyte-gated neuromorphic operation. The IAE-gated organic neuromorphic transistors (IONTs) exhibit exceptional mechanical resilience, maintaining nearly identical electrical properties and synaptic plasticity under 50% strain and after 1000 mechanical stretching cycles in stark contrast to the conventional ion-gel-gated device, which suffers a current drop exceeding two orders of magnitude. Uniquely, by selection and assembly of the gate electrode materials that can be a stretchable carbon nanotube or a flexible gold electrode, we program the IONTs with distinct synaptic plasticity for sensory processing or learning. Utilizing the strategy, we demonstrate high-accuracy classification of handwritten digits and spoken digits using a reservoir computing framework. Our findings establish a stretchable neuromorphic platform wherein functionally distinct synaptic devices can be achieved individually through physical reconfiguration, paving the way for neuromorphic hardware for multi-functional body-conformable artificial intelligence.

New concepts

Our research introduces the concept of a physically reconfigurable neuromorphic platform, enabled by an ion-conductive adhesive elastomer (IAE). This material allows the synaptic plasticity to be programmed simply by attaching different functional gate electrodes after fabrication. This approach fundamentally differs from conventional neuromorphic devices where synaptic functions are permanently "hardwired" during manufacturing, thus limiting their adaptability. Our work decouples device fabrication from functional programming; specifically, the device can be configured to exhibit either short-term or long-term plasticity simply by assembling it with distinct gate electrodes (CNTs or Au). This is enabled by the IAE that simultaneously provides high ionic conductivity for neuromorphic operation and reliable adhesion for physical reconfiguration. This dual-functionality material strategy unlocks a new pathway to develop truly adaptive and multi-functional electronics, where a neuromorphic device can be tailored for diverse computational tasks like sensory processing or memory.

1. Introduction

Wearable electronics are advancing toward continuous and long-term collection of sensory signals by exploiting tissue-like mechanical properties and conformable interfaces.[1,2] For artificial intelligence (AI) to fully utilize such massive sensory inputs in real time, it is crucial to perform energy-efficient, on-device processing directly on the human body. Organic neuromorphic devices are well-suited for this task, offering low power consumption[3–5] and mechanical softness[6–8] that is compatible with biological tissues. To emulate the efficiency and adaptability of biological neural networks, electronic systems must implement precisely tunable synaptic plasticity, which is a cornerstone for task-specific computation and learning.

Among organic neuromorphic platforms, electrolyte-gated organic neuromorphic transistors (ONTs) emulate the ionic signal transmission of biological systems and exhibit tunable synaptic plasticity through material- and device-level engineering, making them well-suited for a wide range of neuromorphic applications.[9–12] Depending on the synaptic decay characteristics,

[a] *Department of Materials Science and Engineering, Seoul National University, Seoul, 08826, Republic of Korea. E-mail: twlees@snu.ac.kr, jysun@snu.ac.kr*
[b] *Research Institute of Advanced Materials, Seoul National University, Seoul, 08826, Republic of Korea*
[c] *Interdisciplinary Program in Bioengineering, Institute of Engineering Research, Soft Foundry, Seoul National University, Seoul, 08826, Republic of Korea*
[d] *SN Display Co., Ltd., Seoul, 08826, Republic of Korea*
† Seung-Woo Lee, Kwan-Nyeong Kim, and Sangjun Ma contributed equally to this work.

ONTs can be tailored for specific functions; devices with short-term plasticity are suited for sensory processing,[1,13–15] while those with long-term plasticity facilitate learning behaviors,[16,17] akin to peripheral and central nervous systems, respectively. This tunability has been achieved through various strategies, including engineering the microstructures of semiconducting polymers[11,18–20] and particularly the choice of gate electrode materials,[21,22] which influence voltage drop and ion migration dynamics *via* differences in polarizability and surface area.[21,23–26] Such approaches have enabled the fabrication of individual devices with specific synaptic characteristics. However, a key limitation persists: once fabricated, the synaptic plasticity of each device is fixed for a specific task, hardwired by its structural configuration. This restricts the adaptability and multifunctionality of neuromorphic systems, especially in wearable applications where compact, integrated, and reconfigurable systems are highly desirable. Moreover, the development of stretchable ONTs that enable physical reconfiguration has been hindered by the lack of suitable gate dielectrics that simultaneously provide high ionic conductivity and reliable interfacial adhesion.

In this work, we introduce a physically reconfigurable organic neuromorphic transistor platform using an ion-conductive adhesive elastomer (IAE) that has both high ionic conductivity and stable interfacial adhesion. Here, we define 'physical reconfigurability' specifically as the capability to modify gate-electrode-induced synaptic behaviors by assembling distinct gate electrodes onto the electrolyte. The IAE, composed of tethered ions and mobile counterions without any liquid components, was adhesive due to abundant ionic groups that enable intrinsic interfacial interactions (Fig. 1a). This enables facile voltage-induced ion migration for electrolyte-gated operation and achieves mechanical integration due to its reliable adhesion with the bonding substrate. This allowed the IAE-gated ONTs (IONTs) to exhibit mechanical resilience even under 50% strain and after 1000 mechanical stretching cycles, maintaining their electrical and synaptic properties. As a key feature, synaptic plasticity could be physically reconfigured by mechanically integrating the IONT with different gate electrodes that were either stretchable carbon nanotube (CNT) electrodes or flexible gold electrodes (Fig. 1b). This approach allowed the function of the individual device using the same channel to be tailored for either sensory processing or learning, respectively. Leveraging this unique reconfigurability, the reservoir computing framework could be constructed by using the IONT to serve as both a physical reservoir and a trainable readout, achieving high-accuracy recognition of handwritten digit images and spoken-digit audio datasets of up to 93.5% (Fig. 1c).

2. Results and discussion

2.1. Design of IAEs for electrolyte-gating of ONTs

We began by evaluating poly(ionic liquid) (PIL)-based elastomers as candidate gate dielectrics for stretchable ONTs, motivated by their potential to form reliable adhesive interfaces due to the intrinsic interfacial interaction, including ion–dipole interactions and hydrogen bonding.[27–30] Although PIL elastomers form a reliable interface within stretchable devices such as sensors and ionic diodes, their application in ONTs has been critically limited due to intrinsically low ionic conductivity, typically ranging from 10^{-7} to 10^{-5} S cm^{-1},[31–34] which restricts efficient ion transport and hinders electrochemical doping of the semiconducting polymer channel.[35,36] Therefore, a key challenge in developing a PIL elastomer-based gate dielectric suitable for ONTs lies in simultaneously achieving high ionic conductivity and intrinsic adhesion. To overcome this, we incorporated a highly polar small molecule, succinonitrile (SN),[37] into a polycationic adhesive elastomer,[33] poly(1-[2-acryloyloxyethyl]-3-butylimidazolium bis(trifluoromethane) sulfonimide) (PAT, Fig. S1 and Table S1) to formulate an IAE.

The ionic conductivity of an IAE with different weight ratios of PAT elastomer to SN was first measured using electrochemical impedance spectroscopy (EIS) (Fig. S2); *i.e.*, 10 : 0 (IAE0), 8 : 2 (IAE2), and 6 : 4 (IAE4). The conductivity systematically increased with SN content, from 1.27×10^{-6} S cm^{-1} in IAE0 to 1.47×10^{-4} S cm^{-1} in IAE2, and 3.74×10^{-4} S cm^{-1} in IAE4, representing an increase of over two orders of magnitude. This originates from the dissociation of ion pairs,[37–39] which facilitates ion migration within the designed IAE, consistent with previously reported plastic-crystalline electrolytes that use SN. By leveraging this design strategy, we effectively addressed the primary challenge of low ionic conductivity, thereby establishing IAEs as suitable gate dielectrics for high-performance IONTs.

We next evaluated the electrolyte-gating efficiency in the IONTs using a blend of poly(3-hexylthiophene) (P3HT) and polystyrene-*block*-poly(ethylene-*ran*-butylene)-*block*-polystyrene (SEBS) as the stretchable semiconducting channel (Fig. 2a).[40] Transfer characteristics of IONTs were measured under standard conditions (the gate voltage V_G: 1.5 V to −3.5 V at 20 mV s^{-1} and drain voltage V_D: −0.5 V). By increasing SN content, the IONTs exhibited a dramatic increase in the maximum drain current I_{max} of IONTs from 0.031 mA (IAE0) to 0.709 mA (IAE2), and up to 1.04 mA (IAE4) (Fig. 2b), highlighting the direct correlation between IAE ionic conductivity and electrolyte gating performance, as higher ion transport enables more effective electrochemical doping of organic channels.[36,41,42] In addition, this over 30-fold improvement in the I_{max} clearly demonstrates the critical role of SN in enabling efficient ion transport and enhancing electrolyte-gating efficiency.

Cyclic voltammetry under voltage sweeps was performed in a 2-electrode configuration to further evaluate the effect of SN addition to the oxidation of the semiconducting polymer (Fig. 2c). Two distinct oxidation peaks were observed for all IAE compositions, which are attributed to the sequential oxidation of the polymer's crystalline and amorphous regions as the potential increases.[43,44] For IAE0, these peaks were located at 1.18 V and 2.08 V. Both peaks systematically shifted to lower potentials, 1.14 V and 1.58 V for IAE2, and 0.75 V and 1.52 V for IAE4, as the SN content increased. In addition, the current density increased gradually and significantly with increasing SN ratio, indicating enhanced ionic penetration and electrochemical doping, which leads to increased charge carrier density in the semiconducting polymer.[11,45–47] This reduction in oxidation peak potentials indicates that the ionic conductivity of the IAE is critical for facilitating the electrochemical

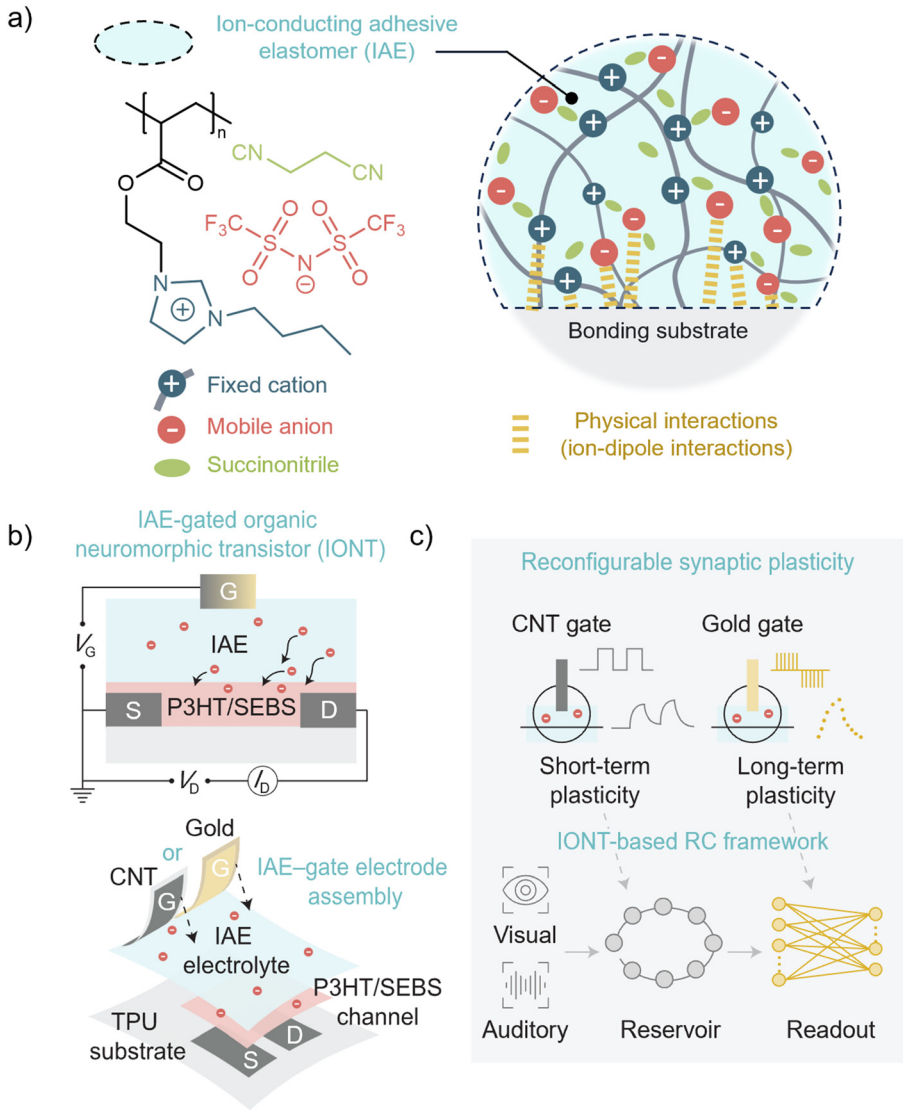

Fig. 1 Conceptual diagram of the IAE-enabled physical reconfiguration of synaptic plasticity. (a) Schematic illustration of the IAE chemical structure, highlighting fixed cations, mobile anions, and succinonitrile additives. Magnified view: interfacial interactions between the IAE and the bonding substrate. (b) Device architecture and the IAE-gate electrode assembly process. The synaptic functionality is physically programmed by laminating either a CNT gate or a gold gate electrode onto the IAE electrolyte. (c) Concept of physically reconfigurable synaptic plasticity and the IONT-based reservoir computing (RC) framework. The CNT gate-attached IONT exhibits short-term plasticity suitable for the physical reservoir, whereas the gold gate-attached IONT demonstrates long-term plasticity suitable for the trainable readout.

doping of semiconducting polymers, consistent with the transistor characterization results.

To investigate the extent of electrochemical doping, *in situ* Raman spectroscopy was performed on transistors comprising P3HT/SEBS active layers, with varying SN content in the IAE (Fig. 2d). The two distinct vibrational modes of P3HT: the intra-ring C=C stretch ($\sim$1444 cm^{-1}) and intra-ring C–C stretch ($\sim$1378 cm^{-1}) were clearly observed in all samples.[48] Upon application of a −3.5 V gate bias for 10 s, all devices exhibited a dramatic redshift in C=C peaks, indicative of oxidation-induced polaron formation in the P3HT chains, which promotes π-electron delocalization and reduces the effective bandgap.[49,50] Notably, the degree of redshift was significantly larger in IAE2 (37 cm^{-1}) and IAE4 (38 cm^{-1}) compared to IAE0 (25 cm^{-1}), directly correlating with the increased ionic conductivity introduced by SN. These results demonstrate that enhanced ion transport in the IAE facilitates more efficient electrochemical doping, thereby accelerating polaron generation in the semiconducting polymer. Consequently, the IONTs exhibit the highest I_{max} (1.04 mA) and transconductance g_m (1.49 mS, Table S1) among reported organic electrochemical transistors utilizing PIL-based dielectrics (Table S2).

We then investigated the adhesion properties of IAEs with varying SN ratios through the 90° peel test and tack test (Fig. 2e and f). First, 90°-peel tests were performed to measure the interfacial toughness, which represents the energy required to propagate delamination between the IAE and the thermoplastic polyurethane (TPU) substrate used as the elastomeric base for

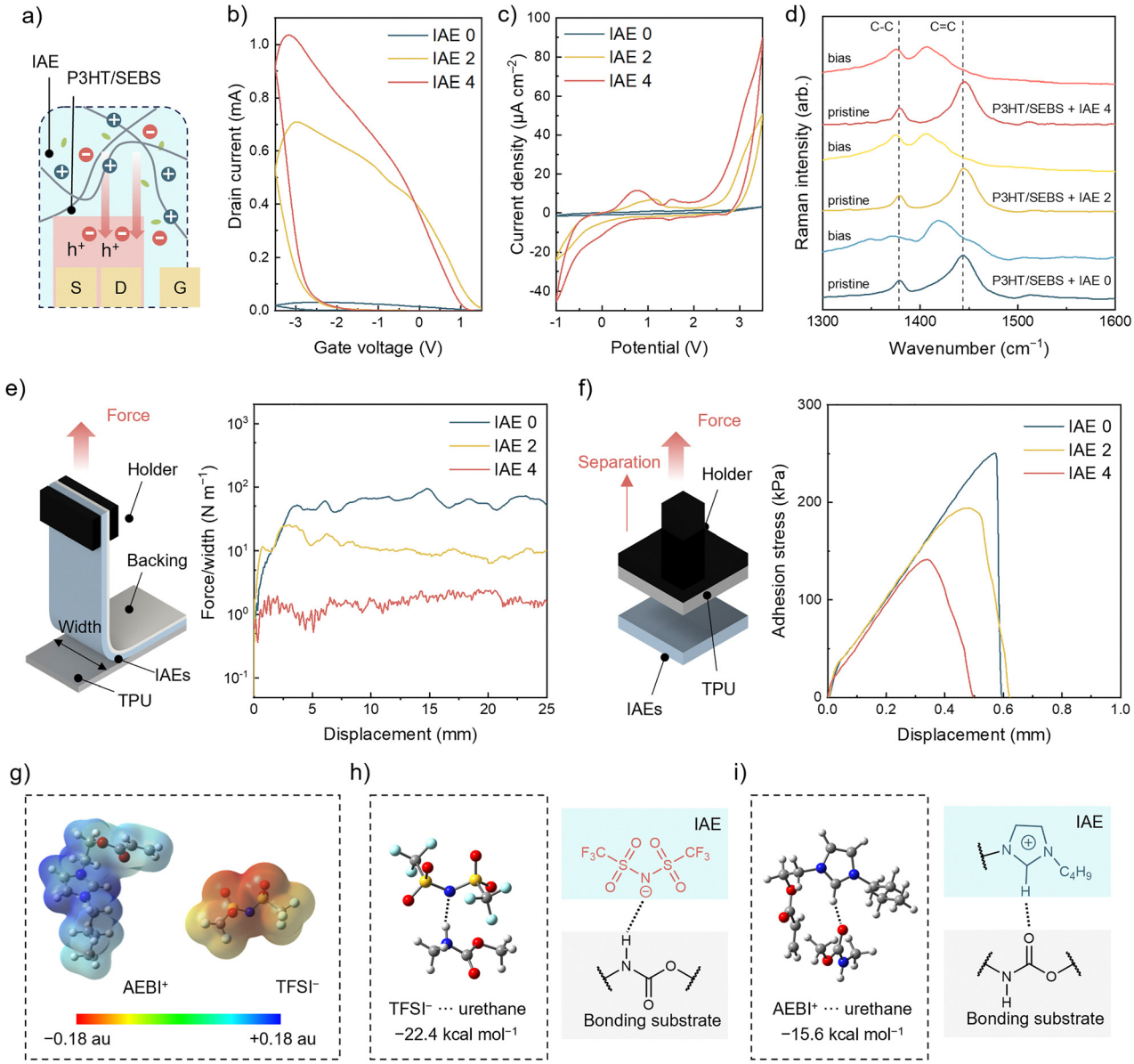

Fig. 2 Design of IAEs for electrolyte-gating of ONTs. (a) Schematic illustration of the electrolyte-gated operation mechanism of the IONT. (b) Transfer curves of IONTs using IAE0, IAE2, and IAE4 as electrolytes. (c) Cyclic voltammetry performed using three IAEs as electrolytes (arrows indicate the oxidation peaks). (d) *In situ* Raman spectra of the P3HT/SEBS channel before and after applying gate bias using three IAEs as electrolytes. (e) 90°-peel test results (force per width *vs.* displacement) of three IAEs on TPU substrates. Schematic: test setup. (f) Tack test results (adhesion stress vs displacement) of three IAEs on a TPU substrate. Schematic: test setup. (g) Electrostatic potential surfaces of $AEBI^+$ and $TFSI^-$, calculated using DFT. Color scale: positive (blue) to negative (red) potential. DFT calculations of binding energies between (h) $TFSI^-$-urethane and (i) $AEBI^+$-urethane with schematic representations of interfacial interactions.

IONTs. The results indicated a systematic decrease in toughness from $\sim$60.7 J m^{-2} for the pure IAE0 to $\sim$1.7 J m^{-2} for IAE4. To complement this, tack tests were conducted to evaluate the adhesion energy, quantifying the force needed for vertical separation after the initial contact. These tests confirmed the same decreasing trend, with values dropping from $\sim$82 J m^{-2} (IAE0) to $\sim$41.4 J m^{-2} (IAE4). We observed that the incorporation of SN induces a trade-off between ionic conductivity and adhesion in the IAE, which is attributed to the reduced density of ionic groups by SN molecules within the polymer matrix. Due to this trade-off, IAE2 was identified as the optimal composition that achieves both high ionic conductivity and intrinsic adhesion, with its adhesion performance significantly surpassing that of the conventional poly(vinylidene fluoride-*co*-hexafluoropropylene) (PVDF-HFP) and 1-ethyl-3-methylimidazolium bis(trifluoromethanesulfonyl)imide ([EMIM][TFSI])-based ion-gel (Fig. S3).

To investigate the origin of the intrinsic adhesion properties of IAEs, density functional theory (DFT) calculations were performed. The surface electrostatic potentials (ESPs) of the constituent monomers of the PAT elastomer, [2-acryloyloxyethyl]-3-butylimidazolium ($AEBI^+$) and bis(trifluoromethane-

sulfonyl)imide ($TFSI^-$), are depicted in Fig. 2g and display extremely positive and negative ESP values, respectively.[52] We then calculated the binding energies of $AEBI^+$ and $TFSI^-$ with the urethane model unit (Fig. 2h and i), which revealed the interactions between each molecule ($TFSI^-\cdots$urethane, binding energy −22.4 kcal mol^{-1}; $AEBI^+\cdots$urethane, binding energy −15.6 kcal mol^{-1}).[53] These results confirm that the reliable adhesion between the IAE and TPU originates from favorable interfacial interactions (ion–dipole interactions and hydrogen bonding) between the abundant ionic moieties in the IAE and the polar urethane groups in the TPU, validating the molecular design of the IAE.[28–30,51] Although the incorporation of SN can compromise this adhesion by reducing the density of ionic groups in the IAE, it simultaneously plays a critical role in significantly enhancing ionic conductivity. Notably, IAE2 retained sufficient interfacial interactions with TPU, maintaining an intrinsic adhesion significantly higher than that of conventional ion gels (Fig. S3). From these material characterization studies, the favorable balance between ionic conductivity and interfacial adhesion positions IAE2 as the most promising candidate to overcome the critical limitation of low ionic conductivity inherent to conventional PIL materials. Yet, the mechanical durability of this material under strain, which is critical for wearable applications, requires systematic quantification based on device failure analysis.

2.2. Mechanical resilience of IONTs

To confirm the mechanical viability of IAE2, which currently presents the most favorable balance of properties for mechanically compliant devices (Fig. 2), a fully-stretchable IONT architecture was developed for systematic characterization of electrical performance under deformation. The IONT was fabricated by spin-coating a P3HT/SEBS blend onto a TPU substrate in which CNT electrodes were embedded and subsequently transferring the IAE onto the channels (Fig. 3a). The detailed fabrication procedure and the reproducibility of the device performance across independent

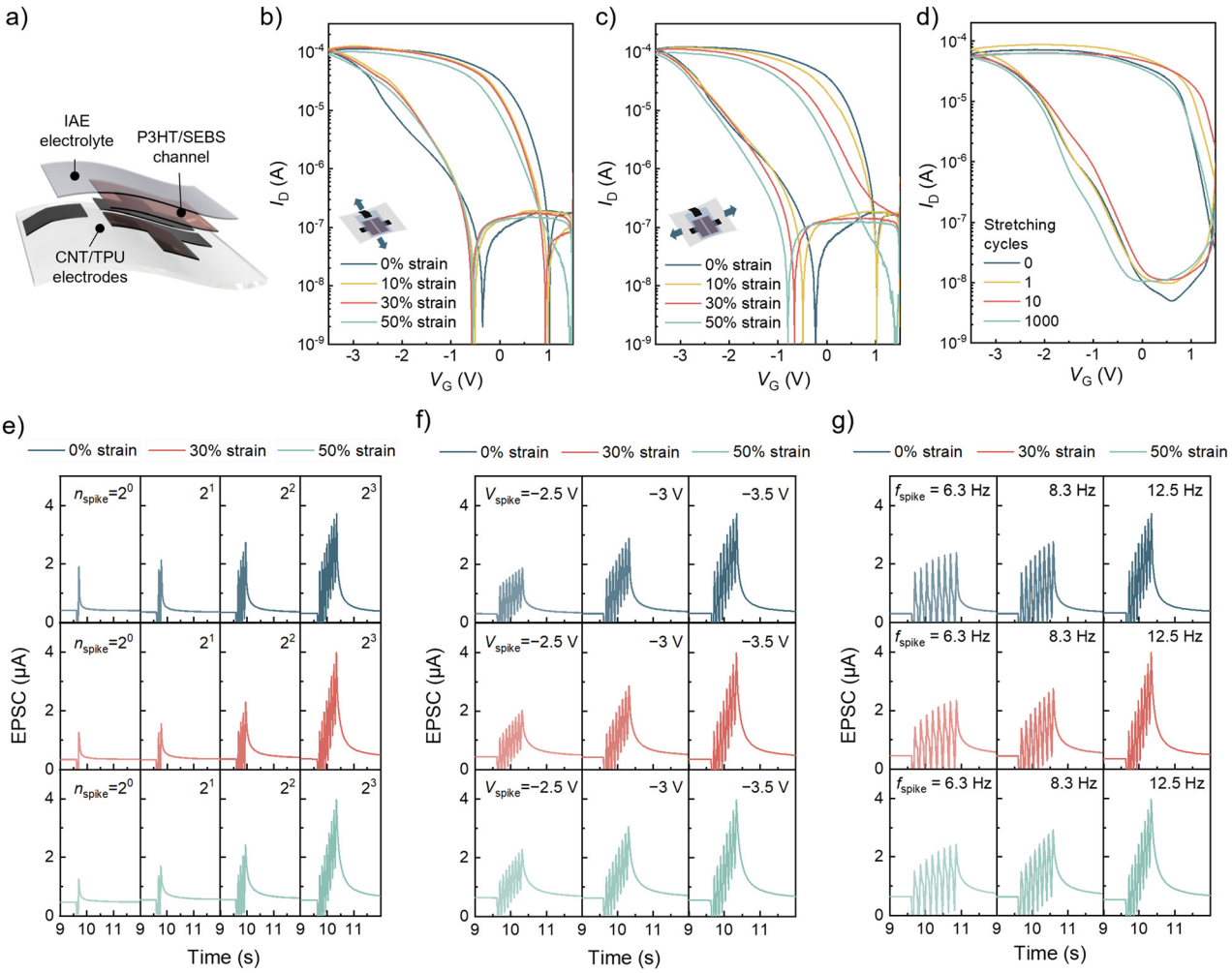

Fig. 3 Electrical and synaptic characteristics of IONTs under mechanical deformation. (a) Schematic illustration of the IONT device structure. Transfer curves of the device under increasing strain applied (b) perpendicular and (c) parallel to the channel length direction. (d) Transfer curves of the device before and after mechanical stretching cycles. Synaptic characteristics of the device from EPSC responses, including (e) spike number-dependent plasticity (SNDP) with 1 to 8 spikes, (f) spike voltage-dependent plasticity (SVDP) with the V_G from −2.5 to −3.5 V, and (g) spike frequency-dependent plasticity (SFDP) with the spike frequency from 6.5 to 12.5 Hz under 0% to 50% strain.

batches are presented in Fig. S4, confirming the reliability of our fabrication scheme. Regarding the channel material, the P3HT/SEBS blend exhibits a favorable mesh-structured phase separation that prevents crack formation even under mechanical deformations,[40] as evidenced by the atomic force microscopy (AFM) and optical microscopy images in Fig. S5.

The transfer characteristics were measured under our standard conditions while applying strain either perpendicular (Fig. 3b) or parallel (Fig. 3c) to the channel length direction. Under a 50% static strain applied perpendicular to the channel, the device exhibited excellent mechanical stability, maintaining 89% of its initial I_{max} (decreasing from 112 μA to 100 μA). Along the parallel direction at 50% strain, the device also maintained 79% of its initial I_{max} (from 121 μA to 96 μA), further demonstrating its mechanical resilience along multiple stretching directions. Furthermore, the device exhibited excellent cyclic durability, retaining ~87% of its initial I_{max} after 1000 mechanical stretching cycles at 30% strain (Fig. 3d). These results highlight that the intrinsic interfacial adhesion of the developed IAE effectively preserves device integrity under mechanical deformation, enabling stable and reliable operation of the IONT even under deformation.

To extend the discussion on material selection from material-level characterization to quantitative verification at the device level, we conducted a comparative analysis of the operational failure modes of IONTs incorporating the high-conductivity IAE4. While IAE4 possesses higher ionic conductivity, its poor adhesion (interfacial toughness of 1.7 J m^{-2}) led to a clear failure mode characterized by interfacial delamination at 30% strain. This is quantitatively demonstrated in Fig. S6, where the IAE4-based device exhibits a sharp drop in the drain current and a loss of gate modulation at this strain. This failure stands in sharp contrast to the stable operation of the IAE2-based device, which maintained robust performance even at 50% strain as shown above. This device-level quantitative analysis confirms that IAE2 represents the optimal material choice for ensuring stable neuromorphic operation under deformation. Additionally, we performed a device-level analysis on ONTs fabricated with the conventional PVDF-HFP/[EMIM][TFSI] ion gel. The results showed a drastic reduction in current by more than two orders of magnitude at strain levels above 30% (Fig. S7). This failure aligns with the poor interfacial toughness (Fig. S3), confirming that the lack of adhesion leads to critical failure mode under strain.

To further validate the capabilities of the optimized IAE2 platform, we investigated its dynamic response speed and scalability. The dynamic response speed of the IONT was characterized using short input voltage spikes, which is critical for real-time neuromorphic perception. The device successfully maintained fundamental synaptic facilitation behaviors even when stimulated by spikes with a duration and interval of 5 ms, confirming its potential for high-speed signal processing (Fig. S8). Furthermore, the scalability and uniformity of the device platform were verified by fabricating a 4 × 4 IONT array (Fig. S9). The array exhibited consistent transfer characteristics across 16 devices as indicated in Fig. S9c.

The synaptic plasticity under mechanical deformation, which is critical for wearable neuromorphic applications, was characterized; spike-number- (SNDP), spike-voltage- (SVDP), and spike-frequency-dependent plasticity (SFDP) (Fig. 3e–g). For SNDP, increasing the number of input voltage spikes (−3.5 V) from one to eight increased the excitatory post-synaptic current (EPSC) from ~1.9 μA to ~3.7 μA. The device also exhibited facilitation in response to spike amplitude and frequency; the EPSC ratio (A_8/A_1) increased from 150% to 210% as the voltage was increased from −2.5 V to −3.5 V (SVDP), and from 140% to 210% as the frequency was increased from 6.3 Hz to 12.5 Hz (SFDP). Remarkably, all of these fundamental synaptic behaviors were robustly maintained, with negligible changes in current levels and spike index, even under 50% strain applied perpendicular to the channel length direction. Furthermore, stable synaptic operations were consistently preserved when strain was applied parallel to the channel direction (Fig. S10), collectively demonstrating the exceptional mechanical resilience and functional integrity of the IONT using an IAE.

2.3. Physically reconfigurable synaptic plasticity for reservoir computing frameworks

To demonstrate the physical reconfigurability and mechanical compliance of synaptic plasticity in IONTs, we first verified the ability of IONTs to maintain structural and functional integrity under various physical configurations. This was demonstrated by the conformal adhesion of IONTs to diverse and complex surfaces, including wavy geometries, a brain replica, and a thin rod (diameter = 2 mm), while preserving mechanical robustness during bending and stretching (Fig. 4a).

Building on this, a post-fabrication strategy was developed to define synaptic behavior. After constructing the multilayered structure consisting of a TPU substrate, CNT source/drain electrodes, a P3HT/SEBS channel, and an IAE2 gate dielectric, synaptic plasticity was configured by selectively assembling different gate electrodes onto the IAE layer. Specifically, a high-surface-area CNT/TPU electrode was employed to induce short-term plasticity (STP), whereas a flat Au thin-film/polyimide (PI) electrode was used to achieve long-term plasticity (LTP). Regarding electrode fabrication, the Au gate was formed by thermal evaporation, resulting in a relatively flat surface morphology. Conversely, the stretchable CNT gate was fabricated by spray-coating a CNT network and subsequently embedding it into a TPU elastomer. As confirmed by scanning electron microscopy (SEM) and AFM analyses (Fig. S11a and b), the dense CNT network remained well-exposed on the contact surface, creating a highly porous interface composed of randomly oriented bundles with a higher surface roughness (R_q = 5.3 nm), standing in sharp contrast to the relatively flat Au electrode (R_q = 2.5 nm). Such morphological distinction directly translates to electrochemical properties; capacitance measurements revealed that the porous CNT electrode possesses a significantly larger specific capacitance (58.9 μF cm^{-2}) compared to the relatively flat Au electrode (4.9 μF cm^{-2}) (Fig. S11c and d). The observed capacitance difference arises because the porous CNT network provides a larger effective surface area for

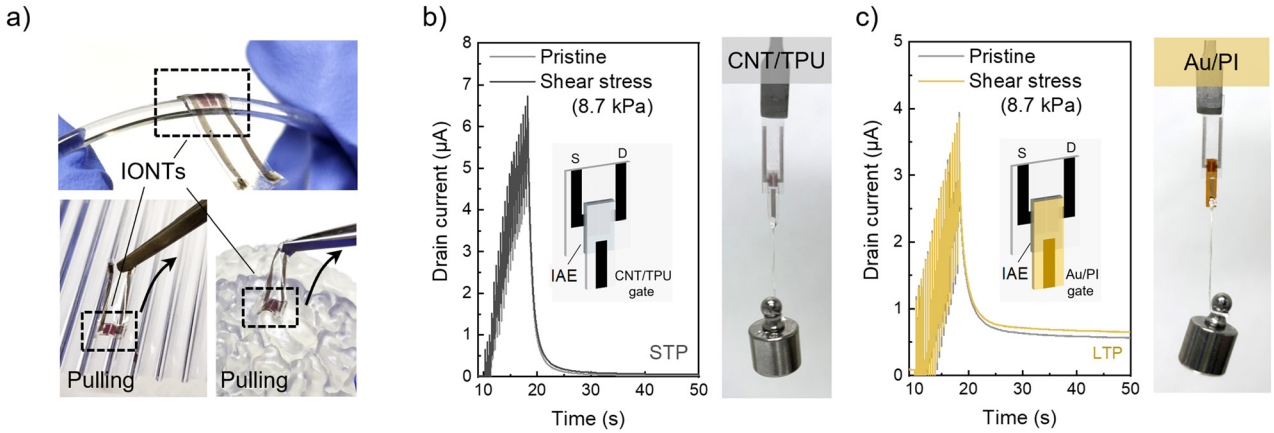

Fig. 4 Gate assembly-defined modulation of synaptic plasticity. (a) Photographs demonstrating the conformal adhesion of IONTs to various complex geometries, including a bent rod (top), a wavy surface (bottom left), and a brain replica (bottom right). (b) Short-term plasticity (STP) behaviors of an IONT assembled with a stretchable CNT/TPU gate electrode. (c) Long-term plasticity (LTP) behaviors of an IONT assembled with a flexible Au/PI gate electrode. The electrical characteristics in (b) and (c) were measured with and without an applied shear stress of 8.7 kPa (load-bearing test), confirming stable synaptic operation under external mechanical loads.

electric double-layer formation compared to the planar Au interface. Consequently, compared to the high-capacitance CNT gate, the relatively smaller capacitance of the Au gate leads to a larger portion of the gate voltage dropping at the gate/electrolyte interface, resulting in the slower withdrawal of ions from the channel, as established in previous reports.[21,23–26]

The modulation of synaptic plasticity and mechanical stability of the physically attached gate electrodes was then assessed through a load-bearing test, where the load was suspended from the assembled gate electrodes. The distinct STP and LTP behaviors of the two reconfigured IONTs were successfully verified, with negligible changes in drain current and synaptic plasticity even under a shear stress of 8.7 kPa (Fig. 4b and c). These results confirm that physical reconfiguration enabled by the IAE can effectively modulate synaptic plasticity while simultaneously ensuring high mechanical stability. Such dual functionality is essential for constructing reliable and intelligent wearable and on-body neuromorphic systems.

This strategy enables the STP and LTP functionalities to be programmed at desired locations, facilitating the construction of neuromorphic computing systems, such as the reservoir computing (RC) framework demonstrated here.[54] The RC framework was built entirely from the reconfigurable IONTs, which could be programmed to implement the different inter-node connection behaviors in reservoir and readout layers (Fig. 5a). The IONT integrated with the CNT gate electrode (STP IONT) was employed as a physical reservoir to process temporal sensory inputs, and the IONT integrated with the Au gate electrode (LTP IONT) functioned as a trainable readout layer, which enabled stable memory and learning capabilities.

For the implementation of reconfigurable IONTs for reservoir and readout layers, they were characterized by applying distinct sets of voltage spikes (Fig. 5b–d). The STP IONT, serving as the physical reservoir, effectively separated the temporal input of 4-bit voltage spike trains (250 ms) into 16 distinct reservoir states (Fig. 5b). This hardware-level preprocessing allows for a reduction in the network size by a factor of four, significantly lowering the subsequent computational cost. The LTP IONT functioned as a trainable readout, demonstrating 50 discrete conductance states in response to a series of potentiation (−3.5 V, 300 ms) and depression (2.2 V, 300 ms) voltage spikes across five consecutive cycles (Fig. 5c), with the corresponding nonlinearity values as indicated in Fig. S12. This capability indicates its ability to update the analog weights for neuromorphic computing. The conductance states were measured at time t = 12 s after voltage spike applications, where $\Delta G = |1 - I(t)/I(t - 0.05\ \mathrm{s})| < 0.5\%$, where $I(t)$ is the current at time t, and $I(t - 0.05\ \mathrm{s})$ is the current at the previous measurement point, with 0.05 s as the interval between successive measurements (Fig. 5d). Finally, the complete reservoir computing framework was validated through simulations on sensory recognition tasks, using the Mixed National Institute of Standards and Technology (MNIST) handwritten digit database and the free spoken-digit dataset (FSDD). For the RC simulation, the characteristics of both reservoir and readout layers were implemented directly from the experimentally measured characteristics of the STP and LTP IONTs (details on the simulation are provided in the Methods section). This approach stands in contrast to previously demonstrated hybrid RC frameworks that rely on software-defined weights, which increases the system complexity and limits their integration potential.[55–57] The framework yielded high classification accuracies of 93.5% for spoken digits and 88.4% for handwritten digit datasets in 30 epochs (Fig. 5e). The confusion matrices further indicated that the trained model successfully classified the digits according to their true labels. This successful demonstration confirms that our reconfigurable IONTs can serve as foundational building blocks for neuromorphic computing, emulating the adaptability and multifunctionality of biological neural networks.

The following aspects of the IAE-based neuromorphic system can be further investigated to enhance its integration and

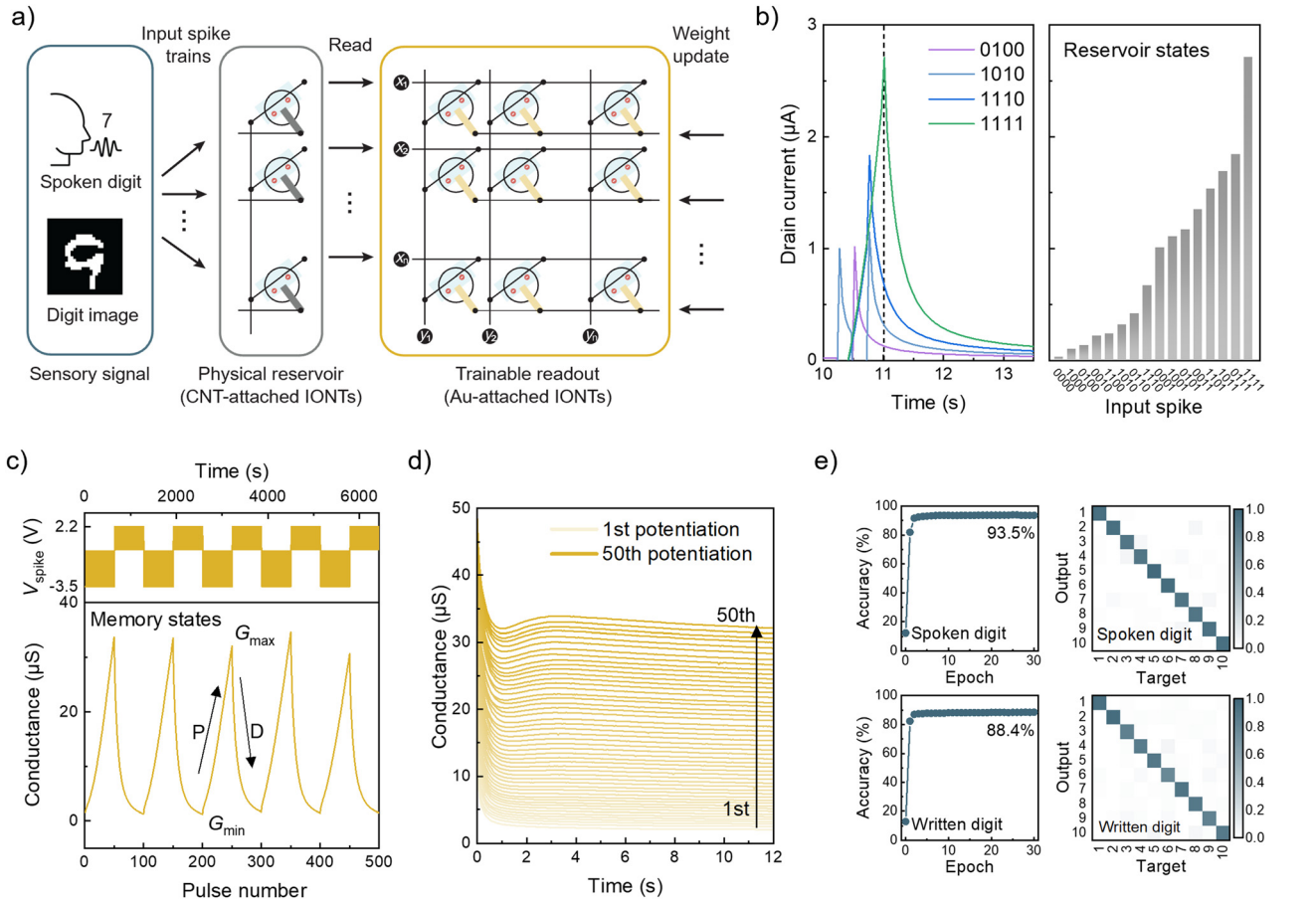

Fig. 5 IONT-based RC framework. (a) Schematic of the RC framework constructed using IONTs (CNT gate-attached for physical reservoir and Au gate-attached for trainable readout). (b) Reservoir states of the CNT gate-attached IONT in response to 4-bit spike trains (selected examples shown). (c) Potentiation and depression characteristics of the Au gate-attached IONT (50 spikes each). G_{max}: maximum conductance state and G_{min}: minimum conductance state. (d) Discrete conductance states programmed during 50 successive potentiation spikes. (e) Classification accuracy and confusion matrices for spoken and handwritten digit recognition tasks.

operational speed. First, high-resolution fabrication processes such as photolithography[58] or inkjet printing[59] can be implemented to effectively improve both synaptic response and device density. Second, surface passivation strategies can be introduced to minimize parasitic capacitance for stable high-frequency operation.[60] Finally, the manual functionalization step can evolve into high-throughput automated assembly, potentially utilizing transfer printing[61] to precisely integrate gate electrode arrays.

3. Conclusions

In summary, we present a stretchable neuromorphic transistor platform with physically reconfigurable synaptic plasticity, overcoming the limitations of conventional ONTs in which synaptic plasticity is hardwired by their structural configuration. This was achieved by designing an IAE gate dielectric layer that simultaneously provides high ionic conductivity for efficient electrolyte-gating operation and intrinsic adhesion for mechanical robustness, thereby enabling post-fabrication reconfiguration of synaptic plasticity through mechanical integration with different gate electrodes. The IONTs exhibited excellent mechanical resilience, maintaining stable electrical and synaptic characteristics by preserving 89% of the I_{max} under 50% strain and 87% after 1000 cycles of mechanical stretching, in stark contrast to the over two-orders-of-magnitude current drop in devices using conventional ion gel gate dielectrics even under only 30% strain. This strategy allowed a single IONT to exhibit either STP or LTP depending on the mechanically attached gate electrode, providing functional versatility that conventional ONTs with fixed configurations cannot offer. Leveraging this approach, we constructed a reservoir computing framework using the reconfigurable IONTs that operate as both a physical reservoir exhibiting STP behavior and a trainable readout exhibiting LTP behavior. This system achieved high recognition accuracy (up to 93.5%) and demonstrated multitasking capability by successfully classifying both visual and auditory sensory inputs. This research demonstrates a significant step towards versatile, body-conformable neuromorphic electronics, laying the foundation for future on-body artificial intelligence systems that are multifunctional, reconfigurable, and seamlessly integrated into daily life.

4. Experimental section

4.1. Materials

2-Bromoethyl acrylate (stabilized with 900–1500 ppm of 4-methoxyphenol) was purchased from Alfa Aesar. The bis(trifluoromethane)sulfonimide lithium salt (Li[TFSI]) and 2,2-dimethoxy-2-phenylacetophenone (DMPA) were purchased from TCI chemicals. Dichloromethane (DCM) and acetonitrile were purchased from Daejung Industry. SEBS (H1221) was purchased from Asahi Kasei. TPU (KA-480) was obtained from Kolon Industries. P3HT (M_w 70–90 kDa) was purchased from Solaris Chem. CNT (P3-SWNT) was purchased from Carbon Solutions. Isopropanol alcohol (IPA) was purchased from Fisher Scientific. [EMIM][TFSI] was purchased from Solvionic. 1-Butylimidazole, poly(ethylene glycol) diacrylate (PEGDA, average Mn 250), SN, trichloroethylene, octadecyltrimethoxysilane (OTS), ammonium hydroxide, PVDF-HFP (average M_n ~130 000), acetone, toluene, tetrahydrofuran (THF), and deionized (DI) water were purchased from Sigma-Aldrich. All chemicals were used as received.

The 1-[2-acryloyloxyethyl]-3-butylimidazolium bis(trifluoromethane) sulfonimide (AT) monomer was synthesized following previously reported procedures.[33,62] 2-Bromoethyl acrylate (5.0 g, 1.0 equiv) was mixed with 1-butylimidazole (3.64 g, 1.05 equiv) in 30 mL of acetonitrile. The reaction mixture was stirred at 60 °C overnight. Upon completion, acetonitrile was removed under reduced pressure using a rotary evaporator. The resulting crude product, 1-[2-acryloyloxyethyl]-3-butylimidazolium bromide ([AEBI]Br), was dissolved in 30 mL of DI water. Subsequently, Li[TFSI] (8.0 g, 1.0 equiv) was added to the aqueous solution, and the mixture was stirred at room temperature overnight to allow anion exchange. The resulting water-insoluble AT monomer was extracted with DCM and washed with DI water at least three times. The organic layer was dried over anhydrous sodium sulfate, and the final product was obtained as a pale yellow liquid after vacuum drying ($<10^{-1}$ Torr).

4.2. IAE electrolyte preparation

The AT monomer was mixed with 2 mol% PEGDA as a crosslinker. Subsequently, 0.5 mol% DMPA dissolved in ethanol (100 mg mL^{-1}) was added as the photoinitiator. The resulting solution was stirred thoroughly, and ethanol was removed under vacuum ($<10^{-1}$ Torr) at room temperature. The viscous mixture was then cast into a polytetrafluoroethylene mold, separated by polyethylene terephthalate spacers. Photopolymerization was carried out by irradiating the sample with 365 nm UV light for 30 min. After curing, unreacted monomers were removed by immersing the cured AT in DCM overnight. The final elastomer was dried in a vacuum oven at 60 °C for 24 h to eliminate any residual solvent.

To prepare IAEs with varying weight ratios of PAT elastomer to SN, the mass of the previously synthesized PAT elastomer was first measured to determine the required amount of SN for each formulation. SN was dissolved in DCM at a weight ratio of 1 : 1.2 (SN : DCM) to prepare a homogeneous solution, which was uniformly applied onto the elastomer. The samples were then sealed in Petri dishes and incubated at 40 °C for 12 h to facilitate diffusion of SN into the polymer network. The resulting materials were optically transparent and exhibited no visible phase separation or crystallized SN domains. To remove the residual solvent, the samples were subsequently dried under vacuum ($<10^{-1}$ Torr) at 40 °C for an additional 2 h.

4.3. Device fabrication

A semiconducting polymer solution was prepared by dissolving P3HT (5 mg mL^{-1} in toluene) and stirring the mixture overnight at 200 rpm and 70 °C. This solution was then mixed with a separate SEBS solution (27 mg mL^{-1} in toluene) at a 65 : 35 weight ratio (P3HT:SEBS) to form the final solution. CNT solution was prepared by dispersing P3-SWNTs in a 9 : 1 (v/v) mixture of IPA and DI water. The mixture was subjected sequentially to bath sonication for 6 h and tip sonication for 30 min, followed by centrifugation at 8000 rpm for 30 min to remove large precipitates.

To investigate the effect of different IAE compositions, a set of IONTs on rigid glass substrates were first fabricated. For these devices, the source, drain, and gate electrodes were formed by thermally evaporating Au (30 nm) with a 5 nm Cr adhesion layer onto a glass substrate *via* a shadow mask (L = 250 μm and W = 3 mm) under high vacuum (≈10^{-6} Torr). The P3HT/SEBS solution was then spin-coated onto the substrate (2000 rpm, 60 s), resulting in a 30 nm thick film, which was subsequently annealed at 100 °C for 30 min in a N_2 atmosphere. The device fabrication was completed by attaching the IAE, which serves as the electrolyte.

The intrinsically stretchable IONTs were fabricated by first preparing a stretchable CNT–TPU electrode film. A hydrophobic OTS self-assembled monolayer was formed on a silicon wafer by spin-coating a 0.1% (v/v) solution of OTS in trichloroethylene at 2000 rpm for 30 s. Then, the wafer was exposed to an ammonium hydroxide atmosphere for 6 h, followed by rinsing with toluene. The CNT dispersion was then spray-coated onto this OTS-treated surface, which was maintained at 150 °C, to define the electrode patterns (L = 250 μm and W = 3 mm). A TPU solution (60 mg mL^{-1} in THF) was then drop-cast and dried at room temperature. The resulting CNT–TPU film was peeled off the wafer and flipped over to serve as the stretchable substrate with the electrodes. The P3HT/SEBS solution was spin-coated (2000 rpm, 60 s) onto to CNT–TPU film using a PI stencil mask to cover the gate electrode area, followed by annealing (100 °C, 30 min, N_2). The IAE electrolyte with a thickness of 100 μm was then attached over the channel and gate area. For the PVDF–HFP ion-gel, a solution of PVDF–HFP, [EMIM][TFSI], and acetone was prepared in a 1 : 2 : 7 weight ratio. The solution was then drop-cast and dried overnight to yield a 100 μm-thick film.

For the physically reconfigured IONTs, the common base devices were fabricated by first forming CNT–TPU source and drain electrodes, followed by spin-coating P3HT/SEBS and attaching the IAE, as described previously. In parallel, two distinct top-gate electrodes for assembly (Au and CNT) were prepared separately: the flexible Au gate was fabricated by thermally evaporating Cr (5 nm) and Au (30 nm) onto a PI film through a shadow mask, while the stretchable CNT gate was prepared by spray coating CNT onto OTS-SiO_2, drop-casting

TPU, and peeling off the resulting CNT–TPU film. Finally, a selected top-gate electrode was gently placed and brought into contact with the IAE surface to finalize the device assembly.

4.4. Characterization

All electrical characteristics of IONTs were measured using a Keysight B1500A semiconductor device parameter analyzer. *In situ* Raman spectroscopy was performed using a LabRAM HR Evolution system with a 785 nm laser wavelength. The Raman spectra were acquired after applying a voltage of −3.5 V for 10 s. EIS measurements were performed using a Novocontrol Concept-40 spectrometer. SEM, AFM, and optical microscopy images were obtained using a SUPRA 55VP (Carl Zeiss), NX-10 (Park Systems), and BX53M (Olympus), respectively. The Peel test and tack test were measured using an Instron 3343 Single-Column Testing System. For the peel test, a thin polyester film was used as a backing layer for the IAE. The sample was then mounted on a TPU substrate and loaded into an Instron universal testing machine. The measurement was conducted by pulling the sample at a speed of 50 mm min^{-1}. The width of the sample was 1 cm. The interfacial toughness was calculated from the steady-state peeling force per unit width in the plateau region. For the tack test, a TPU substrate was applied to an IAE and affixed to it by applying a pressure of 100 kPa for 30 s. The adhesion stress was measured by separating the samples at a speed of 20 mm min^{-1}. The adhesion energy was calculated as the area under the stress–displacement curve. DFT calculations were conducted using Gaussian 09W software, with geometry optimization performed using b3lyp/6-311g(d,p), including the atom-pairwise dispersion correction with Becke–Johnson damping, and binding energy calculated as $E_{Binding} = E_{AB} - E_A - E_B$, where E_A, E_B, and E_{AB} stand for the energy of component A, component B, and the complex of A and B, respectively.

4.5. Reservoir computing simulation

All simulations were conducted in a Python 3.7 environment utilizing the open-source CrossSim Ver 2.0 simulator (https://github.com/sandialabs/cross-sim/releases/tag/v2.0, Sandia National Laboratory). The neural network architecture comprises a physical reservoir layer replicating the voltage spike train response of the STP-IONT device, coupled to a trainable single-layer perceptron (SLP) readout. For the handwritten digit recognition (MNIST) task, each 28 × 28 pixel image was encoded into 196 spike trains by segmenting the data into 4-pixel blocks. For the spoken-digit recognition task using the publicly available FSDD,[63] raw audio files were preprocessed into 64 × 80 pixel cochleagrams using the Lyons hearing model; these were normalized, binarized, and subsequently segmented into 1280 spike trains. These spike trains were fed into the physical reservoir. The resulting reservoir states were read by the SLP readout layer, which was configured with dimensions of (196 × 10) for the MNIST task and (1280 × 10) for the FSDD task. The output neurons utilized the softmax activation function. The network was trained using a stochastic gradient descent algorithm with a batch size of 1024. Weight updates were determined by mapping calculated gradients to a conductance lookup table generated from the actual potentiation/depression characteristics of the LTP IONT devices. The MNIST task utilized 60 000 training and 10 000 test images, while the FSDD task employed 2400 training and 600 test samples.

4.6. Informed consent statement

Informed consent was obtained from the human subject involved in the photographic demonstration shown in Fig. S9b. The subject is one of the authors, S.-W. Lee, and the procedure was limited to a non-invasive visual demonstration without any physiological data collection.

Conflicts of interest

There are no conflicts to declare.

Data availability

The data supporting this article have been included as part of the supplementary information (SI). Supplementary information is available. See DOI: https://doi.org/10.1039/d5mh01319d.

Acknowledgements

This research was supported by the Pioneer Research Center Program through the National Research Foundation of Korea funded by the Ministry of Science, ICT & Future Planning (2022M3C1A3081211). This research was also supported by the Nano & Material Technology Development Program through the National Research Foundation of Korea funded by the Ministry of Science and ICT (RS-2024-00416938).

References

1 Y. Lee, Y. Liu, D.-G. Seo, J. Y. Oh, Y. Kim, J. Li, J. Kang, J. Kim, J. Mun, A. M. Foudeh, Z. Bao and T.-W. Lee, *Nat. Biomed. Eng.*, 2023, **7**, 511–519.
2 N. Li, Y. Li, Z. Cheng, Y. Liu, Y. Dai, S. Kang, S. Li, N. Shan, S. Wai, A. Ziaja, Y. Wang, J. Strzalka, W. Liu, C. Zhang, X. Gu, J. A. Hubbell, B. Tian and S. Wang, *Science*, 2023, **381**, 686–693.
3 Y. van de Burgt, A. Melianas, S. T. Keene, G. Malliaras and A. Salleo, *Nat. Electron.*, 2018, **1**, 386–397.
4 C. D. Schuman, S. R. Kulkarni, M. Parsa, J. P. Mitchell, P. Date and B. Kay, *Nat. Comput. Sci.*, 2022, **2**, 10–19.
5 Y. Lee, H.-L. Park, Y. Kim and T.-W. Lee, *Joule*, 2021, **5**, 794–810.
6 S.-W. Lee, S. Kim, K.-N. Kim, M.-J. Sung and T.-W. Lee, *Biosens. Bioelectron.*, 2024, **261**, 116444.
7 S. Dai, Y. Dai, Z. Zhao, F. Xia, Y. Li, Y. Liu, P. Cheng, J. Strzalka, S. Li, N. Li, Q. Su, S. Wai, W. Liu, C. Zhang, R. Zhao, J. J. Yang, R. Stevens, J. Xu, J. Huang and S. Wang, *Matter*, 2022, **5**, 3375–3390.
8 D.-G. Seo, G.-T. Go, H.-L. Park and T.-W. Lee, *MRS Bull.*, 2021, **46**, 321–329.

9 M.-J. Sung, K.-N. Kim, C. Kim, H.-H. Lee, S.-W. Lee, S. Kim, D.-G. Seo, H. Zhou and T.-W. Lee, *Chem. Rev.*, 2025, **125**, 2625–2664.
10 H. Park, Y. Lee, N. Kim, D. Seo, G. Go and T. Lee, *Adv. Mater.*, 2020, **32**, 1903558.
11 M. Sung, D. Seo, J. Kim, H. E. Baek, G. Go, S. Woo, K. Kim, H. Yang, Y. Kim and T. Lee, *Adv. Funct. Mater.*, 2023, 2312546.
12 K. Kim, M. Sung, H. Park and T. Lee, *Adv. Electron. Mater.*, 2022, **8**, 2100935.
13 Y. Lee, J. Y. Oh, W. Xu, O. Kim, T. R. Kim, J. Kang, Y. Kim, D. Son, J. B.-H. Tok, M. J. Park, Z. Bao and T.-W. Lee, *Sci. Adv.*, 2018, **4**, eaat7387.
14 Y. Kim, A. Chortos, W. Xu, Y. Liu, J. Y. Oh, D. Son, J. Kang, A. M. Foudeh, C. Zhu, Y. Lee, S. Niu, J. Liu, R. Pfattner, Z. Bao and T.-W. Lee, *Science*, 2018, **360**, 998–1003.
15 G. Go, Y. Lee, D. Seo and T. Lee, *Adv. Mater.*, 2022, **34**, 2201864.
16 I. Krauhausen, D. A. Koutsouras, A. Melianas, S. T. Keene, K. Lieberth, H. Ledanseur, R. Sheelamanthula, A. Giovannitti, F. Torricelli, I. Mcculloch, P. W. M. Blom, A. Salleo, Y. van de Burgt and P. Gkoupidenis, *Sci. Adv.*, 2021, **7**, eabl5068.
17 Y. van de Burgt, E. Lubberman, E. J. Fuller, S. T. Keene, G. C. Faria, S. Agarwal, M. J. Marinella, A. Alec Talin and A. Salleo, *Nat. Mater.*, 2017, **16**, 414–418.
18 D.-G. Seo, Y. Lee, G.-T. Go, M. Pei, S. Jung, Y. H. Jeong, W. Lee, H.-L. Park, S.-W. Kim, H. Yang, C. Yang and T.-W. Lee, *Nano Energy*, 2019, **65**, 104035.
19 G.-T. Go, Y. Lee, D.-G. Seo, M. Pei, W. Lee, H. Yang and T.-W. Lee, *Adv. Intell. Syst.*, 2020, **2**, 2000012.
20 N. Kim, G.-T. Go, H.-L. Park, Y. Ahn, J. Kim, Y. Lee, D.-G. Seo, W. Lee, Y.-H. Kim, H. Yang and T.-W. Lee, *Adv. Intell. Syst.*, 2023, **5**, 2300016.
21 C. Kim, D. G. Roe, D. U. Lim, Y. Y. Choi, M. S. Kang, D.-H. Kim and J. H. Cho, *Sci. Adv.*, 2024, **10**, eadn6217.
22 S. Wang, Y. Wang, X. Cai, B. Wang, C. Zhao, G. Pan, C. Harder, Y. Bulut, B. Zhang, S. Zhang, Y. Kong, K. Huang, B. Xie, P. Müller-Buschbaum, S. V. Roth, L. Yang, Y. Li, Y. Han, G. Bao and W. Ma, *Nat. Electron.*, 2025, **8**, 254–266.
23 G. Tarabella, C. Santato, S. Y. Yang, S. Iannotta, G. G. Malliaras and F. Cicoira, *Appl. Phys. Lett.*, 2010, **97**, 123304.
24 D. A. Koutsouras, F. Torricelli, P. Gkoupidenis and P. W. M. Blom, *Adv. Mater. Technol.*, 2021, **6**, 2100732.
25 K. G. Cho, K. H. Lee and C. D. Frisbie, *ACS Appl. Mater. Interfaces*, 2024, **16**, 19309–19317.
26 O. Larsson, A. Laiho, W. Schmickler, M. Berggren and X. Crispin, *Adv. Mater.*, 2011, **23**, 4764–4769.
27 H. Pei, H. Hu, Y. Dong, H. Zhu, C. Zhang, Y. Zhou, J. Huang, S. Shi, Z. Wang, X. Wu and W. Huang, *Adv. Funct. Mater.*, 2025, **35**, 2506431.
28 S. Huang, Y. Wan, Y. Sun, K. Zhang, X. Ming, H. Zhu, Q. Zhang and S. Zhu, *ACS Appl. Polym. Mater.*, 2022, **4**, 3217–3224.
29 J. Zhang, Z. Chen, Y. Zhang, S. Dong, Y. Chen and S. Zhang, *Adv. Mater.*, 2021, **33**, 2100962.
30 Y. Zheng, H. Ning, B. Zhao, Y. Jiang, J. Chen, Y. Wu, D. Nie, X. Hu, Z. Yan, R. Xie, C. Shi and N. Lin, *Adv. Mater.*, 2025, **37**, 2417175.
31 Y. Peng, L. Gao, C. Liu, H. Guo, W. Huang and D. Zheng, *Small*, 2025, **21**, 2409384.
32 J.-H. Choi, W. Xie, Y. Gu, C. D. Frisbie and T. P. Lodge, *ACS Appl. Mater. Interfaces*, 2015, **7**, 7294–7302.
33 H. J. Kim, B. Chen, Z. Suo and R. C. Hayward, *Science*, 2020, **367**, 773–776.
34 Y. He, Y. Cheng, C. Yang and C. F. Guo, *Nat. Mater.*, 2024, **23**, 1107–1114.
35 T. J. Quill, G. LeCroy, A. Melianas, D. Rawlings, Q. Thiburce, R. Sheelamanthula, C. Cheng, Y. Tuchman, S. T. Keene, I. McCulloch, R. A. Segalman, M. L. Chabinyc and A. Salleo, *Adv. Funct. Mater.*, 2021, **31**, 2104301.
36 C. G. Tang, R. Wu, Y. Chen, Z. Zhou, Q. He, T. Li, X. Wu, K. Hou, C. J. Kousseff, I. McCulloch and W. L. Leong, *Adv. Mater.*, 2024, **36**, 2405556.
37 P.-J. Alarco, Y. Abu-Lebdeh, A. Abouimrane and M. Armand, *Nat. Mater.*, 2004, **3**, 476–481.
38 W. Chae and T. Earmme, *Gels*, 2024, **10**, 798.
39 D. Bao, W. Zhao, Z. Li, Y. Tao, Y. Zhong, Z. Tang, Z. Gao, H. Wang, H. Zhang and X. Sun, *J. Energy Storage*, 2024, **91**, 112016.
40 Y.-S. Guan, F. Ershad, Z. Rao, Z. Ke, E. C. da Costa, Q. Xiang, Y. Lu, X. Wang, J. Mei, P. Vanderslice, C. Hochman-Mendez and C. Yu, *Nat. Electron.*, 2022, **5**, 881–892.
41 K. Hou, S. Chen, R. A. John, Q. He, Z. Zhou, N. Mathews, W. S. Lew and W. L. Leong, *Adv. Sci.*, 2024, **11**, 2405902.
42 S. Chen, Z. Zhou, K. Hou, X. Wu, Q. He, C. G. Tang, T. Li, X. Zhang, J. Jie, Z. Gao, N. Mathews and W. L. Leong, *Nat. Commun.*, 2024, **15**, 7056.
43 J. Nightingale, C. Pitsalidis, A.-M. Pappa, E. Tan, K. Stewart, R. M. Owens and J.-S. Kim, *J. Mater. Chem. C*, 2020, **8**, 8846–8855.
44 J. K. Harris, B. Neelamraju and E. L. Ratcliff, *Chem. Mater.*, 2019, **31**, 6870–6879.
45 W. Kim, K. Lee, S. Choi, E. Park, G. Kim, J. Ha, Y. Kim, J. Jang, J. H. Oh, H. Kim, W. Jiang, J. Yoo, T. Kim, Y. Kim, K.-N. Kim, J. Hong, A. Javey, D. Rha, T.-W. Lee, K. Kang, G. Wang and C. Park, *Nat. Mater.*, 2025, 1–10.
46 J. Guo, S. E. Chen, R. Giridharagopal, C. G. Bischak, J. W. Onorato, K. Yan, Z. Shen, C.-Z. Li, C. K. Luscombe and D. S. Ginger, *Nat. Mater.*, 2024, **23**, 656–663.
47 S. T. Keene, C. Lubrano, S. Kazemzadeh, A. Melianas, Y. Tuchman, G. Polino, P. Scognamiglio, L. Cinà, A. Salleo, Y. van de Burgt and F. Santoro, *Nat. Mater.*, 2020, **19**, 969–973.
48 H. Zheng, Y. Liu, H. Ma, Y. Wang, G. Zhou, Z. Cao and K. Xu, *Polymer*, 2025, **321**, 128089.
49 K. Stewart, K. Pagano, E. Tan, M. Daboczi, M. Rimmele, J. Luke, S. Eslava and J.-S. Kim, *Adv. Mater.*, 2024, **36**, 2211184.
50 J. Nightingale, J. Wade, D. Moia, J. Nelson and J.-S. Kim, *J. Phys. Chem. C*, 2018, **122**, 29129–29140.
51 S. Sun, J. Liu, Q. Yue, J. Lv, S. Wang and Y. Wei, *Macromolecules*, 2024, **57**, 9355–9366.
52 J. Liu, S. Gan, D. Yang, Q. Yue, S. Sun, M. Wu, X. Li, G. Chang and Y. Wei, *Chem. Eng. J.*, 2024, **491**, 151967.
53 D. Gao, G. Thangavel, J. Lee, J. Lv, Y. Li, J.-H. Ciou, J. Xiong, T. Park and P. S. Lee, *Nat. Commun.*, 2023, **14**, 1990.

54 X. Liang, J. Tang, Y. Zhong, B. Gao, H. Qian and H. Wu, *Nat. Electron.*, 2024, **7**, 193–206.
55 D. Liu, X. Tian, J. Bai, S. Wang, S. Dai, Y. Wang, Z. Wang and S. Zhang, *Nat. Electron.*, 2024, **7**, 1176–1185.
56 S. Dai, X. Zhang, X. Liu, X. Tian, B. Cui, I. Pang, H. Luo, D. Liu, X. He, X. Chen, J. Zhang, Z. Wang, J. Huang and S. Zhang, *Adv. Mater.*, 2025, **37**, 2413951.
57 Y. Zhong, J. Tang, X. Li, X. Liang, Z. Liu, Y. Li, Y. Xi, P. Yao, Z. Hao, B. Gao, H. Qian and H. Wu, *Nat. Electron.*, 2022, **5**, 672–681.
58 Y.-Q. Zheng, Y. Liu, D. Zhong, S. Nikzad, S. Liu, Z. Yu, D. Liu, H.-C. Wu, C. Zhu, J. Li, H. Tran, J. B.-H. Tok and Z. Bao, *Science*, 2021, **373**, 88–94.
59 F. Molina-Lopez, T. Z. Gao, U. Kraft, C. Zhu, T. Öhlund, R. Pfattner, V. R. Feig, Y. Kim, S. Wang, Y. Yun and Z. Bao, *Nat. Commun.*, 2019, **10**, 2676.
60 G. Frusconi, Z. M. Kovács-Vajna, P. W. M. Blom, P. Gkoupidenis and F. Torricelli, *Adv. Mater. Technol.*, 2025, **10**, 2401440.
61 K. Sim, S. Chen, Z. Li, Z. Rao, J. Liu, Y. Lu, S. Jang, F. Ershad, J. Chen, J. Xiao and C. Yu, *Nat. Electron.*, 2019, **2**, 471–479.
62 H. Shin, J. Shin, R. C. Hayward and H. J. Kim, *Macromolecules*, 2023, **56**, 7827–7836.
63 Z. Jackson, C. Souza, J. Flaks, Y. Pan, H. Nicolas and A. Thite, *Jakobovski/free-spoken-digit-dataset (version v1.0.8) Zenodo*, 2018.